Article

A Theoretical Study of SRPK Interaction with the Flexible Domains of Hepatitis B Capsids

Jehoon Kim[1] and Jianzhong Wu[1,*]
[1]Department of Chemical and Environmental Engineering, University of California, Riverside, California

ABSTRACT   Hepatitis B virus (HBV) controls genome encapsidation and reverse transcription from a single-stranded RNA to a double-stranded DNA through the flexible C-terminal domain (CTD) of the capsid proteins. Although the microscopic structure of the nucleocapsid plays a critical role in the life cycle of HBV, the location of CTD residues at different stages of viral replication remains poorly understood. In this work, we report the radial distributions of individual amino-acid residues of the CTD tails for both empty and RNA-containing HBV capsids by using a coarse-grained model for the key biological components and the classical density functional theory. The density functional theory calculations reveal substantial exposure of the CTD residues outside the capsid, in particular when it is devoid of any nucleic materials. The outermost layer of the capsid surface mainly consists of residues from ^{170}Ser-^{175}Arg of the CTD tails, i.e., the serine-arginine protein kinase binding motif. The theoretical description corroborates recent in vitro studies that show a transient CTD distribution captured by serine-arginine protein kinase binding. We have also investigated the nucleocapsid structural changes due to phosphorylation of serine residues and shown a correlation between the CTD location and the internal distribution of RNA segments.

INTRODUCTION

Hepatitis B virus (HBV) is a human pathogen infecting around 2 billion people worldwide. Acute and chronic HBV infection may cause serious dysfunctions including liver fibrosis, cirrhosis, and cancer (1). The HBV virion, also known as Dane particle, has a double-shelled structure consisting of surface proteins and nucleocapsid (NC) containing a circular partially double-stranded DNA (dsDNA). The HBV capsid is formed by the self-assembly of the capsid proteins with a pregenomic RNA (pgRNA) and the viral polymerase (Pol), a reverse transcriptase for transformation of pgRNA to dsDNA (2–4). Each NC has an icosahedral structure with triangulation number T = 3 or 4. T4 is the major form (95%) in vivo, which is made of 240 copies of the core protein (CP) (5–7). A wild-type (WT) CP has 183 amino-acid (aa) residues, including an assembly domain (1–140 aa), a nonapeptide linker (141–149 aa), and the C-terminal domain (CTD, 150–183 aa). The assembly domain has a rigid structure that contributes to the capsid scaffold. However, both the linker and the CTD chains are flexible; the latter is referred to as protamine tails because they are rich in arginine residues (8,9).

It has been long recognized that CTD plays an essential role in the life cycle of HBV infection (8). The HBV capsid is fenestrated with symmetrical pores that allow mass transport and the extrusion of the CTD tails (10–12). The exposure of the CTD tails affects genome packaging, nuclear entry, as well as capsid envelopment and egress (8,13,14).

In addition, it has been recognized that the CTD tails are involved in signaling capsid maturation (15–17). Because CTD exposure alters the surface properties of the NC particle, its location at different stages of replication is critical to differentiate the mature and immature NCs. If the CTD chains were truncated by mutation, the CPs would be unable to encapsidate the full content of the pgRNA, generating capsids with a smaller amount of DNA or empty capsids (8). In addition, each CTD chain has three phosphorylation sites (S155, S162, and S170) important for RNA encapsidation and reverse transcription (8,13). For the WT virus, the CTD chains are phosphorylated at the early stage of replication (with pgRNA or intermediate DNA) (14), but dephosphorylated for matured capsids (with dsDNA) (18,19). Replacing three serine residues with charged amino acids affects pgRNA encapsidation and DNA synthesis. For example, a phosphorylated analog, with one serine residue replaced by glutamic acid, is able to package the pgRNA but fails to support viral DNA replication (13). Meanwhile, substantial reduction of RNA packaging was observed by substitution of serine with aspartic acid (20,21). The CTD chains are also important in viral replication because only phosphorylated capsids were allowed to transport into cellular nucleus (22). Despite such significance, the kinase responsible for the CTD phosphorylation remains little known. Because all phosphorylated serine residues at CTD are followed by repeated arginine residues, serine/arginine protein kinase (SRPK) was suggested as one of the candidates (23,24). It has been demonstrated experimentally that SRPK is effective to phosphorylate capsid proteins in vitro (25).

To clarify how CTD chains regulate genome evolvement as well as intracellular trafficking of HBV capsids (16,22), it is imperative to determine the spatial distribution during different stages of replication. Regrettably, experimental detection of the CTD structure has been elusive. Whereas the assembly domain of HBV capsids maintains a relatively rigid structure, CTD chains are highly flexible and their structure is changing in response to the evolving genome (15,22,26–29). Recently, the enzymatic recognition of SRPK was used to analyze the location of CTD tails (30). The in vitro experiments for the binding affinity of SRPK with HBV capsids indicate that the CTD tails are exposed at the surface when the capsid does not contain any nucleic materials. Conversely, the CTD tails are mainly distributed inside the capsid for the RNA-containing nucleocapsids (30). Regrettably, the CTD chains were not visible through a conventional microscopy such as cryo-electron microscopy (cryo-EM) (7,31). Only a few recent studies capture a trace amount of CTD chains through reconstructed EM images (29,32). Besides, HBV capsids expressed in *Escherichia coli* contain the bacterial RNA instead of pgRNA (22,25,29,30,33). The in vitro assembly of HBV capsids typically occurs at an electrolyte concentration much larger than that corresponding to the physiological condition. The high salinity is required not only to avoid capsid aggregation but also to maintain the thermodynamic stability of the reassembled capsids (25). Although DNA-containing viral particles are available from expression in mammalian cells at physiological conditions, a discrete separation of the capsids at each maturation state is currently impracticable. Detection of the capsid structure is also complicated by the intracellular environmental effects (34).

Previously, we developed a theoretical platform for predicting the microscopic structure and thermodynamic properties of HBV nucleocapsids using a coarse-grained (CG) model for the key viral components and the classical density functional theory (DFT) (35,36). Our model predicted a quantitative relationship between the CTD length and the genome content in good agreement with experimental data. In this work, we apply the same model to locate the SRPK binding motif by analyzing its affinity with HBV capsids at different distributions of the CTD tails. Specifically, we consider CTD distributions in HBV capsids either with or without RNA as examined in recent experiments (29). In addition, we study the structural reorganization of RNA chains due to CTD phosphorylation.

MOLECULAR MODEL AND METHODS

As in our previous work (35,36), we use a CG model to account for nonspecific interactions among the key ingredients of the HBV capsid, i.e., RNA and CTD chains in an electrolyte background. Whereas the atomistic details, including the secondary structure of RNA, are unquestionably important to the biological functions and the kinetics of encapsidation, the essential features of the genome packaging and its interaction with the flexible domains of the capsid proteins are mainly affiliated with electrostatic interactions and molecular excluded volume effects. The nature of nonspecific interactions can be justified by the fact that HBV capsids expressed in *E. coli* have RNA content similar to that in the WT capsids (12).

In our theoretical calculations, the electrostatic interactions and molecular excluded-volume effects are described with tangentially connected chains of hard spheres that each corresponds to one amino-acid residue or nucleotide. We assume that all RNA segments have the same diameter, $\sigma_R = 0.75$ nm, and electrostatic valence of $Z_R = -1$ (37). The diameter of CTD segments, $\sigma_T = 0.5$ nm, reflects the average van der Waals diameter of amino-acid residues (38). The electrical charge corresponds to the characteristic value of each amino-acid residue under physiological condition, and is assigned with the valence of $+1$, 0, and -1. Specifically, $Z = +1$ is assigned to arginine, -1 for glutamate, and all other residues carry no net charge.

The primitive model of electrolyte solutions is used to describe salt ions and water molecules in the background. As in the experimental work (29), the surrounding environment for the HBV capsids is represented by a NaCl solution at concentration of 0.14 M. Approximately, Na$^+$ and Cl$^-$ have the diameters of $\sigma_{Na} = 0.39$ nm and $\sigma_{Cl} = 0.36$ nm, respectively, and the dielectric constant for water is 78.4 (39). The pair potential between ions includes a hard-sphere repulsion and a Coulomb energy:

$$\beta u_{ij}(r) = \begin{cases} \infty, & r < \sigma_{ij} \\ \dfrac{z_i z_j l_B}{r}, & r \geq \sigma_{ij} \end{cases}, \qquad (1)$$

where $\beta = 1/k_B T$, k_B is the Boltzmann constant, $T = 298$ K, $\sigma_{ij} = (\sigma_i + \sigma_j)/2$, and $l_B = 0.714$ nm is the Bjerrum length. Equation 1 is also applied to the pair interaction between the polymeric segments. The bonding potential between the CG RNA segments is described by the Dirac δ-function:

$$\exp[-\beta V_{RNA}(R)] = \prod_{i=1}^{M-1} \frac{\delta(|r_{i+1} - r_r| - \sigma_R)}{4\pi \sigma_R^2}, \qquad (2)$$

where M is the degree of polymerization, and $R = (r_1, r_2, \cdots r_M)$ specifies the positions of monomeric segments. The CTD tails (and 9 aa linkers) are also modeled as tangentially connected spheres of the same size but different valences.

As mentioned previously, the HBV capsids are fenestrated with pores ~1.5 nm in diameter, allowing the permeation of salt ions and CTD tails but not the RNA genome

(11,33,40). The inner and outer radii of the capsid are $R_{in} = 13$ nm and $R_{out} = 15$ nm, respectively (41). The confinement effect for the RNA segments can be described as a spherical cavity with a hard-wall potential

$$\phi_{RNA}(r) = \begin{cases} \infty, & r > R_{in} - \dfrac{\sigma_R}{2} \\ 0, & \text{otherwise} \end{cases}. \qquad (3)$$

The linker-CTD tails are partially confined with the first linker segment tethered at the inner surface of the capsid. Whereas certain capsid pores are more favorable for tail permeation (11,33,40), we estimate the overall probability (10%) considering the approximated ratio of total pore area to inner capsid area. Accordingly, we set an external potential for the tail segments,

$$-\beta\phi_{Tail}(r) = \begin{cases} \ln(0.1), & R_{in} - 0.5\,\sigma_T < r < R_{out} + 0.5\,\sigma_T \\ 0, & \text{otherwise} \end{cases}. \qquad (4)$$

We assume the charges on the capsid are uniformly distributed over a spherical surface located at $r = 15$ nm. The small ions are distributed either inside or outside the HBV capsid. According to previous investigations (42,43), the charge density of the capsid is $Q_c = 0.7\ e\,/\,nm^2$, where e denotes the unit charge. The linker-CTD tails are tethered on the inner capsid surface.

Application of the DFT to electrolyte solutions and polymers has been well documented (44–47). In our previous work (35,39), we showed that the DFT performs well for the electrostatic interactions and the excluded volume effects. The Supporting Material details the equations used in the DFT calculations.

RESULTS

Empty capsid versus RNA-containing NC

We consider first the radial distributions of the polymeric segments and small ions for empty and RNA-containing capsids. Fig. 1 shows the schematic structure of empty capsid and nucleocapsid. In DFT calculations, the HBV capsid is depicted as a spherical shell (the dashed lines) of 2 nm in thickness, corresponding to the average diameter of a capsid dimmer. The CG RNA, CTD of capsid proteins are shown as tangentially connected spheres, and the salt ions are shown as black and red dots. Accordingly to experiments, the CTD tails are primarily exposed outside the empty capsid, whereas the formation of RNA-NC complex severely restricts their exposure.

The DFT calculations provide the density profiles of polymeric segments and small ions. Fig. 2 shows that, in the absence RNA, the CTD chains distribute like that of a typical polymer brush on both sides of the capsid. The oscillatory density profile within the protein shell reflects the molecular excluded volume effects amplified by an artificial wall potential. The distributions of small ions outside the capsid surface constitute an electric double layer (EDL), i.e., a strong accumulation of counterions accompanied by depletion of coions. Different from a typical EDL, however, the counterions are not directly in contact with the surface charge. Instead, counterion accumulation arises mainly from the CTD brush distributed inside the capsid. Within the CTD brush, the counterion density is significantly lower than the density of polymer segments. As a result, it swells significantly more in comparison with a normal polyelectrolyte brush (48). The concentrations of cations and anions are nearly identical at the capsid center, where the salt concentration is virtually the same as that in the bulk solution.
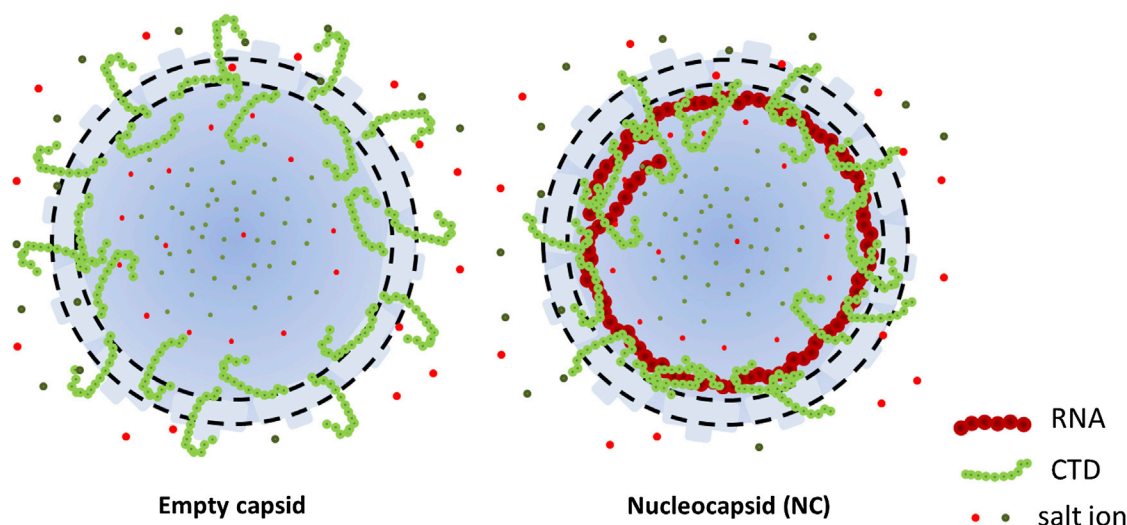

FIGURE 1 Schematic representations of empty and RNA-containing HBV capsids. To see this figure in color, go online.
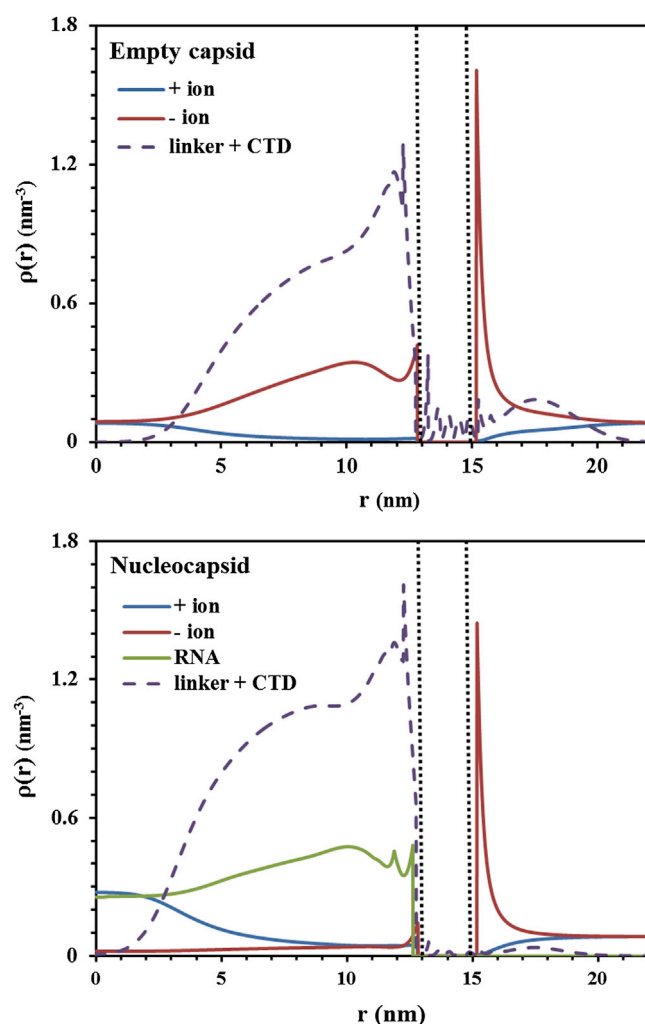
FIGURE 2 The radial distributions of polymeric segments in empty and RNA-containing HBV capsids. The density profiles of salt ions, segments of linker-CTDs, and RNA chains are shown for the empty capsid (*A*) and the nucleocapsid (*B*). In this and other figures, the perpendicular dotted lines indicate the inner and outer positions of the capsid surface. To see this figure in color, go online.

Because the CTD chains are tethered near the capsid pores, they do not contribute to the Donnan equilibrium. As a result, there is no uneven distribution of free ions far from the capsid shell.

Fig. 2 *b* shows the radial distributions of polymeric segments and small ions within the RNA-containing capsid. Interestingly, encapsidation of the RNA chain does not lead to significant changes in the density profiles of cations and anions within the EDL at the capsid out surface. However, the CTD brush outside the NC virtually disappears, indicating that the CTD tails are mostly confined within the NC due to the strong electrostatic attraction between RNA and CTD chains. The microscopic structure of the NC inside is also quite different from that of the empty capsid. First of all, the counterions within the CTD brush are virtually replaced by the RNA segments. Indeed, the

counterions are almost depleted as one may expect from the Donnan equilibrium. Because the CTD chains are mostly confined with the capsid, the brush in NC is slightly thicker than that in the empty capsid. Because the CTD chains are rather extended within the NC, the RNA segments distribute almost uniformly within the brush. Such structure inside the NC cannot be detected with conventional cryo-EM methods but probably measureable with neutron or x-ray scattering.

The location of CTD residues

A recent in vitro study of HBV structure by Chen et al. (30) indicates that the CTD chains are exposed outside the capsid shell for empty capsids, whereas they are confined inside the capsid for RNA-containing NCs. By analyzing CTD interaction with the surrounding molecules in the solution, Chen et al. provided additional information for the specific sequence of exposed CTD segments. Motivated by these in vitro results for the HBV structure, we have examined the density profiles for the individual segments of the CTD tails.

The DFT allows us to determine the distributions of individual residues of the CTDs. The distribution data may be analyzed in several ways. Here, we first consider the accumulated number of linker-CTD residues as a function of the radial distance r from the capsid center. The sum of all residues at each radial distance is normalized by the total number of amino acid residues, namely, 240. Except for the first tail segment, 42 of the linker-CTD segments are traced, thus the accumulated number of CTD residues changes from 0 to 42 as r increases. For the empty capsid (Fig. 3 *a*), the accumulated number of CTD residues is ~29 at the inner capsid wall ($r = 13$ nm) and 30 at the outer surface ($r = 15$ nm). Accordingly, 30 residues are on average located inside the empty capsid, and 12 residues are exposed outside. However, for RNA-containing NC (Fig. 3 *b*), the accumulated number of linker-CTD residues is ~40 at the outer surface ($r = 15$ nm), indicating that only 2 CTD residues are distributed outside the capsid ($r > 15$ nm). At $r \sim 19$ nm from the center of the NC, the accumulated number of linker-CTD residues approaches 42. For the empty capsid (Fig. 3 *a*), CTD residues are distributed further from the capsid center (up to $r = 22$ nm). These theoretical results suggest how the surface characters are different between the empty and NC due to the extruded CTD residues. We have also considered the distribution data in terms of charged or neutral amino acid groups but find not much variation between the empty and RNA-containing capsids.

Fig. 4 compares the exposed ratio of individual CTD segments. A segment is 100% of exposure if it is fully distributed in the outer region of the capsid, i.e., $r \geq 17$ nm. We assume that the residues in the outer region are able to fully interact with surrounding molecules like cellular enzymes. For convenience, we rank each residue according to its position at the CTD chain, i.e., 1 represents the amino acid
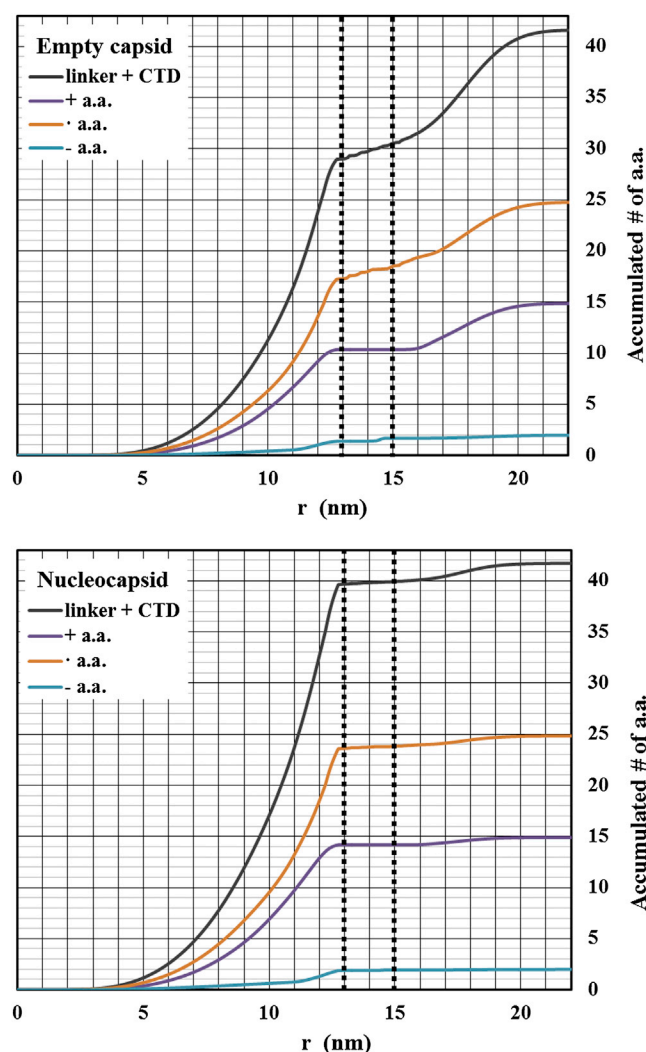
FIGURE 3 The accumulated number of CTD residues for the empty (*a*) and RNA-containing (*b*) HBV capsids. The accumulated number is obtained from a radial integration of the density profiles shown in Fig. 2 for the linker-CTD residues and normalized by the number of overall CTD tails ($N_t = 240$). In other words, the *y* axis corresponds to the summed number of residues per CTD tail up to the radial distance (*r*) from the capsid center. As *r* increases, the summed value approaches 42, which is the total number of traced residues for each tail. The accumulated values for charged (+ and −), neutral (·) residue groups are shown separately. To see this figure in color, go online.
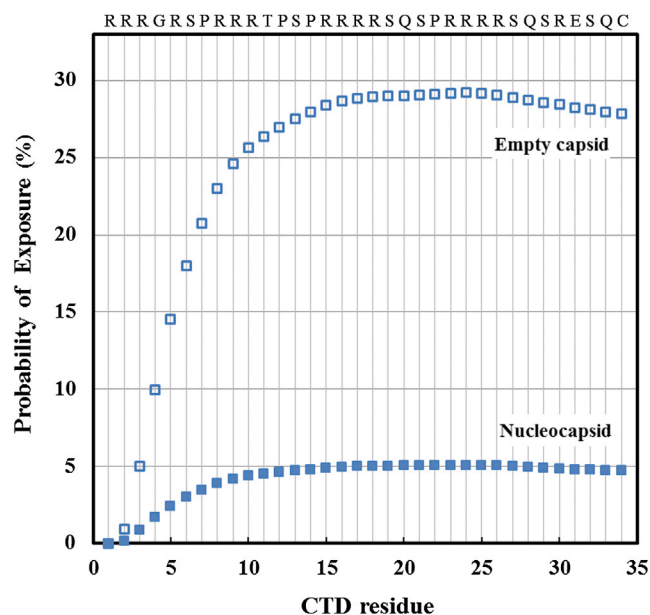

FIGURE 4 The ratio of the exposed CTD residues exposed to the outer region of HBV capsids. The CTD residues exposed in the region $r \geq 17$ nm are counted for both the empty capsid and nucleocapsid. Each residue is ranked from the tethering site (1) to the end segment (34), and the panel above denotes amino-acid residues. To see this figure in color, go online.

tethered at the inner capsid surface, and 34 is the C-terminal residue. As expected, the empty capsid shows higher overall CTD exposure compared to the NC. Assuming that the RNA content is mainly responsible for the deviation between the empty capsid and the NC, we find that the attraction between CTDs and RNA internalizes more than half of the exposed CTD segments in the empty capsid. In the latter case, the exposed ratio peaks around the 21–26th residues (^{170}Ser-^{171}Pro-^{172}Arg-^{173}Arg-^{174}Arg-^{175}Arg), which overlap with a typical binding motif of SRPK (49,50).

Schematically, Fig. 5 depicts the distribution of CTD residues for the empty capsid according to our DFT calcula-

tions. Because the end residues have a lower exposure rate than the 21–26th residues, a CTD tail must somehow bend in the middle, making it have a hook-like shape. The bent structure increases the possibility of the motif to contact with the SRPK. According to our DFT predictions, ~30% present of the residues in such motif are within the reach of the SRPK kinase.

The in vitro study by Chen et al. (30) indicated the transient CTD location in HBV capsids. It revealed the association of SRPK on the outer surface of the empty capsid, mediated by the enzyme-binding motif in the CTD. The same assay was conducted for the NC containing RNA genome but in that case, the enzyme binding was mostly inhibited. The SRPK binding demonstrated unequivocally that the surface characteristics of the capsid changed with the CTD location. Corresponding to the experimental approach, the DFT results capture the transient feature of the capsid surface, rendering additional evidence on the interaction of CTD with SRPK.

The effect of phosphorylation

The CTD distribution is sensitive to the phosphorylation of serine (S) residues (29). In WT capsids, three of the serine residues (S155, S162, S170) have been recognized as phosphorylated upon the capsid formation and packaging with pgRNA (8,13). In our DFT calculations, phosphorylation can be studied simply by setting the valence of those three serine residues from 0 to −1 for the phosphorylated case.
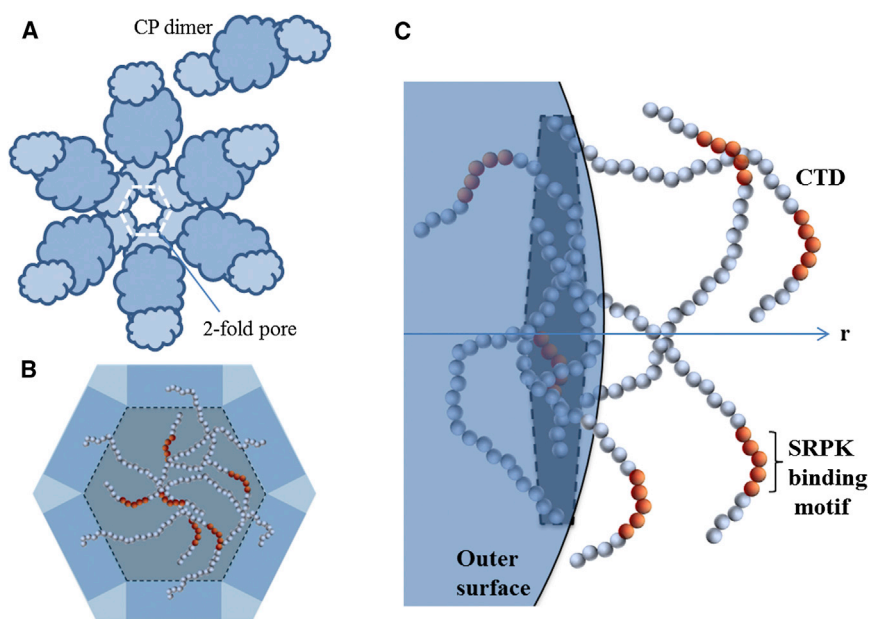
FIGURE 5 Schematic representation of the CTD location. (*A*) Twofold capsid pore and a dimer of the capsid CP. (*B*) 6 CTD tails in each twofold pore. (*C*) CTD tails of the empty capsid. Here, the tails are distributed both inside and outside the empty capsid through the twofold hole. Red segments indicate the SRPK-binding motif. To see this figure in color, go online.

The addition of negative charges affects both the RNA distribution and the exposure of CTD chains.

Fig. 6 shows that the RNA structure inside the capsid varies significantly in response to CTD phosphorylation. Compared to the unphosphorylated case, the RNA segments become more uniformly distributed and are positioned closer to the capsid surface. CTD phosphorylation makes the RNA distribution transduced to have a relatively higher peak near the capsid surface. Phosphorylation reduces the extend CTD exposure outside the capsid. Because the addition of negative charge reduces intrachain electrostatic repulsion, the CTD brush is slightly collapsed in comparison to the unphosphorylated brush.

DISCUSSION

Implication of the CTD exposure

Several recent investigations presented the transient exposure of CTDs to the capsid surface (16,22,27,41,51,52). It has been postulated that the exposed CTDs regulate the posttranslational process of HBV core, i.e., the trafficking into nucleus and the enveloped secretion. Kann et al. (53) determined the fraction of the exposed CTDs for NC in different maturation stages, and suggested the CTD-associated signal modulates the capsid delivery into cellular nucleus. Ning et al. (34) observed that the secreted HBV particles contained either empty capsids or NC with double-stranded DNA, whereas the immature NCs, i.e., those filled with pgRNA or single-stranded DNA, were excluded from secretion. Accordingly, a hypothesis was set such that the immature NCs negatively regulate the trafficking process (29,30,34). Zlotnick's group compared the structural characteristics of empty and RNA-NC, and suggested

that the strong interaction of CTDs with RNA genome obstructs the CTD exposure.

Our theoretical model supports the mechanism of genome-regulated exposure of CTDs. Although we are not describing the whole process of HBV replication, a substantial structural change of CTD implies its functional correlation with the maturation signaling. Our model predicts that about 10 residues for each CTD tail (34 residues) are exposed outside the capsid when the tails are free from the genome contents. Thus, ~30% of CTD segments additionally extruding outside would modify the capsid surface characteristics, which trigger the cellular trafficking. For empty capsids, the CTD tails have been suggested to extrude into far space from the capsid center, so that the outermost reachable r is ~19 nm for RNA-NC but ~22 nm for the empty capsid. Such a structural deviation between empty and RNA-filled capsid supports the hypothesis that the degree of CTD exposure may trigger selective selection upon the posttranslational process (29,30,34). The hypothesis, specifically, the rationale on the transient CTD structure, was also endorsed by experiments (29,30). In supporting those observations, our model gives evidence on the CTD exposure and accessibility into outer capsid space.

Structural changes associated with CTD phosphorylation

It was postulated that HBV carries serine residues in different phosphorylation states during the process of the capsid assembly and reverse transcription of the genome. Specifically, in a duck hepatitis B virus, the capsid proteins (CP) were in phosphorylated form upon the capsid assembly. However, they were dephosphorylated for the mature
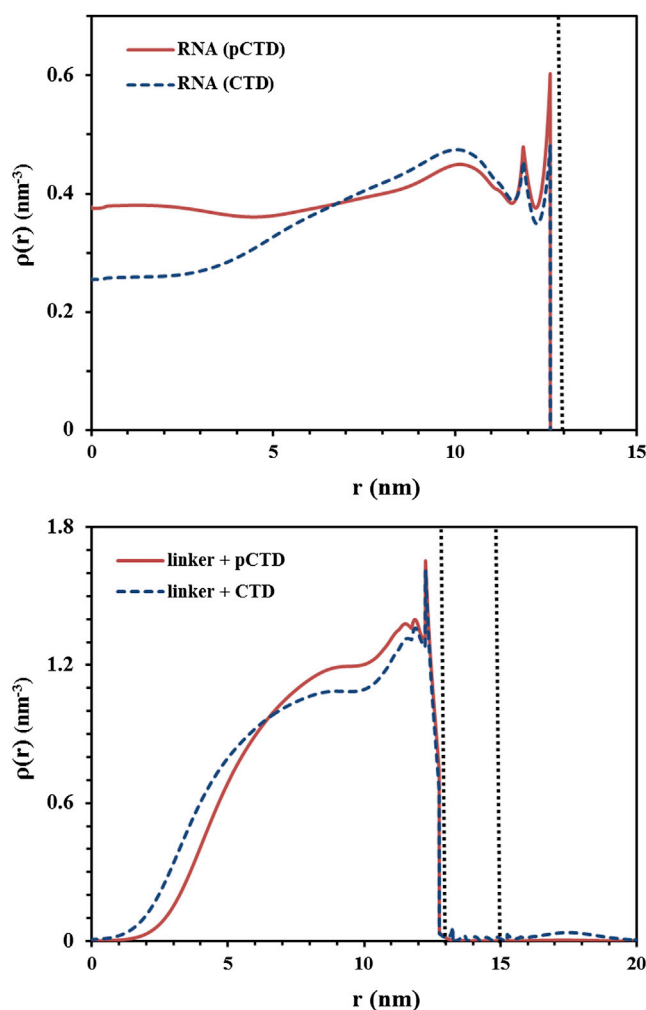
FIGURE 6 Effect of phosphorylation on the distributions of RNA and linker-CTD tails. (*A*) RNA distribution in phosphorylated (pCTD) and unphosphorylated (CTD) capsids. (*B*) The distributions of phosphorylated (pCTD) and unphosphorylated CTD tails. To see this figure in color, go online.

from capsid center, and the inner shell (<7 nm) distribution of the phosphorylated CTDs is relatively depleted. It is expected that the RNA-CTD interaction would be reduced because of added negative charges to the CTD by the phosphorylation. Fig. 6 shows such retarded complex formation between RNA and CTDs. At the inside region ($r < 7$ nm), density profile of RNA for the phosphorylated case is higher than that for the unphosphorylated one. However, corresponding densities of CTD segments for each case are inversed at the region, thus the unphosphorylated CTD chains show higher segmental density than phosphorylated CTD chains. In other words, CTD chains stay relatively apart from the RNA when they gain additional negative charges by the phosphorylation. Accordingly, phosphorylation results in higher RNA density close to the inner surface of the capsid, and it maintains monotonic radial distribution except near the inner wall. By contrast, RNA in the unphosphorylated case shows more inhomogeneous distribution.

Exposure of SRPK-binding motif in the CTD

Although the primary kinase responsible for HBV phosphorylation is still under active investigation, SRPK has been a well-speculated candidate (24,56). SRPK is able to fulfill the in vitro phosphorylation of HBV CPs (24). Moreover, the binding of this enzyme to every twofold pores of HBV empty capsid has been reported (30).

Our DFT calculation provides the density distributions of individual CTD segments in HBV capsids. We find that a specific motif, 21–26th CTD residues of the CTD, is located in the outer region ($r \geq 17$ nm) with the highest probability. Such a serine/arginine repeats domain serves as an ideal substrate for SRPK binding and nuclear localization signals (57,58). At the physiological condition ($C_s = 0.14$ M), the exposure fraction of SRPK-binding motif is expected to be ~30% of that corresponding to the empty capsid. A recent in vitro HBV study showed the empty capsid was decorated by SRPKs at all of the twofold capsid pores. However, RNA-NC failed in that binding assay, indicating that CTDs were not substantially exposed to be accessible for outside SRPKs (30). Regarding the exposure of kinase binding motif, the deviation between the empty capsid and the NC has been confirmed by our DFT calculation. In the presence of the RNA, the exposed fraction of SRPK-binding motif of 21–26th CTD segments is reduced to ~5%.

Chen et al. (30) claimed that no interaction between RNA-NCs and SRPKs were observed in conducting a chromatography of a capsids sample into the SRPK bound column. However, our theoretical model predicts that CTD chains are also partially exposed in RNA-containing NCs but in a relatively much smaller portion. One explanation for this discrepancy is that the enzyme binding requires sufficient substrate contact as for the case of the empty capsids. For RNA-containing NCs, the target motif exposure is

NC filled with relaxed circular DNA (18,54). The CTD in the phosphorylation state is believed to control the pgRNA encapsidation as well as the reverse transcription. Mutation of phosphorylation sites on CTD to mimic unphosphorylation hindered RNA packaging (20,21,55). Similar mutation studies showed CTD phosphorylation affects DNA synthesis (14,21,55). We have investigated the structural effect of phosphorylation. The DFT calculation shows that CTD phosphorylation induces RNA segments to be more localized toward the inner capsid surface (Fig. 6). Such a RNA structure alteration was observed by Wang et al. (29). In the phosphorylation-mimic case, the pgRNA inside the capsid shows more ordered structure than that in *E. coli*-derived nucleocapsid. Our theoretical analysis indicates that such a structural ordering of RNA is correlated with the CTD location. In the phosphorylated state, more of the CTDs are localized at the region between 7 and ~12 nm

insufficient to retain capsids bound on the column. Also in experiment, the RNA-NCs were obtained from the *E. coli* system, filled with the host RNA. Although the bacterial RNA contents have been regarded to mimic the authentic pgRNA regarding its amount (7), their characteristics can be different (59). Accordingly, we assume that the trapped bacterial RNA induces relatively stronger interaction with CTDs than pgRNA. The calculation shows that if the size of RNA in the NC model is set to have larger value than that of the authentic pgRNA (3.5 kb), the CTD exposure ratio decreases (data not shown). It was observed by Rabe et al. (15) that the structure of *E. coli*-derived capsids and authentic immature capsids were clearly different. In their analysis, RNA-NCs were obtained in vivo with inhibiting the reverse-transcription to maintain the pgRNA. A certain portion of CTDs was exposed outside the capsid, therefore cleaved by outside digesting enzyme. However, NCs obtained by expressing the capsid protein in *E. coli* were not affected by outside enzyme, suggesting their CTDs were not exposed.

Even for *E. coli*-derived nucleocapsid with RNA, it was speculated that a certain portion of CTDs are exposed. Vanlandschoot el al. (60) observed the CTD-mediated attachment of nucleocapsids to glycosaminoglycans expressed on the plasma membranes of cells. A recent structural analysis showed that a small portion of CTDs were stretched out through NC pores (32). These results lead to hypothesize that RNA-filled NCs also carry the exposed CTDs but its fraction is substantially small compared to the empty capsid. DFT calculation supports that hypothesis with quantified comparisons. The distinct structures of capsids suggest that the CTD location, specifically, the distribution of the kinase target motifs can be modulated in response to the inside genome. Thus, the phosphorylation process should be entangled with the genome contents by the CTD involvement.

CONCLUSIONS

To summarize, we proposed a CG model to describe the radial distributions of the flexible domains of HBV capsids and encapsidated RNA segments. The molecular model captures the molecular excluded volume effects and electrostatic interactions among the key viral components. The predicted density profiles for the C-terminal domains of the capsid protein (CTD) agree well with experiments, supporting the hypothesis of CTD exposure outside the RNA-free HBV capsids. The DFT predictions validate the important role of CTD location in signaling viral maturation. Furthermore, the theoretical model predicts the most probable position of a SRPK-binding motif in the CTD in good agreement with recent experiment. In addition, we provided a theoretical description for the reorganization of RNA and CTD distributions in response to phosphorylation.

SUPPORTING MATERIAL

REFERENCES

1. WHO 2004. Hepatitis B vaccines. *Wkly. Epidemiol. Rec.* 79:255–263.

2. Hirsch, R. C., J. E. Lavine, …, D. Ganem. 1990. Polymerase gene products of hepatitis B viruses are required for genomic RNA packaging as well as for reverse transcription. *Nature.* 344:552–555.

3. Seeger, C., and W. S. Mason. 2000. Hepatitis B virus biology. *Microbiol. Mol. Biol. Rev.* 64:51–68.

4. Summers, J., and W. S. Mason. 1982. Replication of the genome of a hepatitis B-like virus by reverse transcription of an RNA intermediate. *Cell.* 29:403–415.

5. Kenney, J. M., C. H. von Bonsdorff, …, S. D. Fuller. 1995. Evolutionary conservation in the hepatitis B virus core structure: comparison of human and duck cores. *Structure.* 3:1009–1019.

6. Zlotnick, A., N. Cheng, …, P. T. Wingfield. 1996. Dimorphism of hepatitis B virus capsids is strongly influenced by the C-terminus of the capsid protein. *Biochemistry.* 35:7412–7421.

7. Zlotnick, A., N. Cheng, …, P. T. Wingfield. 1997. Localization of the C-terminus of the assembly domain of hepatitis B virus capsid protein: implications for morphogenesis and organization of encapsidated RNA. *Proc. Natl. Acad. Sci. USA.* 94:9556–9561.

8. Nassal, M. 1992. The arginine-rich domain of the hepatitis B virus core protein is required for pregenome encapsidation and productive viral positive-strand DNA synthesis but not for virus assembly. *J. Virol.* 66:4107–4116.

9. Petit, M. A., and J. Pillot. 1985. HBc and HBe antigenicity and DNA-binding activity of major core protein P22 in hepatitis B virus core particles isolated from the cytoplasm of human liver cells. *J. Virol.* 53:543–551.

10. Bartenschlager, R., and H. Schaller. 1992. Hepadnaviral assembly is initiated by polymerase binding to the encapsidation signal in the viral RNA genome. *EMBO J.* 11:3413–3420.

11. Watts, N. R., J. F. Conway, …, P. T. Wingfield. 2002. The morphogenic linker peptide of HBV capsid protein forms a mobile array on the interior surface. *EMBO J.* 21:876–884.

12. Bruss, V. 2007. Hepatitis B virus morphogenesis. *World J. Gastroenterol.* 13:65–73.

13. Lan, Y. T., J. Li, …, J. Ou. 1999. Roles of the three major phosphorylation sites of hepatitis B virus core protein in viral replication. *Virology.* 259:342–348.

14. Lewellyn, E. B., and D. D. Loeb. 2011. Serine phosphoacceptor sites within the core protein of hepatitis B virus contribute to genome replication pleiotropically. *PLoS ONE.* 6:e17202.

15. Rabe, B., A. Vlachou, …, M. Kann. 2003. Nuclear import of hepatitis B virus capsids and release of the viral genome. *Proc. Natl. Acad. Sci. USA.* 100:9849–9854.

16. Schmitz, A., A. Schwarz, …, M. Kann. 2010. Nucleoporin 153 arrests the nuclear import of hepatitis B virus capsids in the nuclear basket. *PLoS Pathog.* 6:e1000741.

17. Lewellyn, E. B., and D. D. Loeb. 2011. The arginine clusters of the carboxy-terminal domain of the core protein of hepatitis B virus make pleiotropic contributions to genome replication. *J. Virol.* 85:1298–1309.

18. Perlman, D. H., E. A. Berg, …, J. Hu. 2005. Reverse transcription-associated dephosphorylation of hepadnavirus nucleocapsids. *Proc. Natl. Acad. Sci. USA.* 102:9020–9025.

19. Basagoudanavar, S. H., D. H. Perlman, and J. Hu. 2007. Regulation of hepadnavirus reverse transcription by dynamic nucleocapsid phosphorylation. *J. Virol.* 81:1641–1649.

20. Gazina, E. V., J. E. Fielding, …, D. A. Anderson. 2000. Core protein phosphorylation modulates pregenomic RNA encapsidation to different extents in human and duck hepatitis B viruses. *J. Virol.* 74:4721–4728.

21. Köck, J., M. Nassal, …, F. von Weizsäcker. 2004. Hepatitis B virus nucleocapsids formed by carboxy-terminally mutated core proteins contain spliced viral genomes but lack full-size DNA. *J. Virol.* 78:13812–13818.

22. Kann, M., B. Sodeik, …, A. Helenius. 1999. Phosphorylation-dependent binding of hepatitis B virus core particles to the nuclear pore complex. *J. Cell Biol.* 145:45–55.

23. Kau, J. H., and L. P. Ting. 1997. A serine-kinase-containing protein complex interacts with the terminal protein domain of polymerase of hepatitis B virus. *J. Biomed. Sci.* 4:155–161.

24. Daub, H., S. Blencke, …, M. Cotten. 2002. Identification of SRPK1 and SRPK2 as the major cellular protein kinases phosphorylating hepatitis B virus core protein. *J. Virol.* 76:8124–8137.

25. Porterfield, J. Z., M. S. Dhason, …, A. Zlotnick. 2010. Full-length hepatitis B virus core protein packages viral and heterologous RNA with similarly high levels of cooperativity. *J. Virol.* 84:7174–7184.

26. Schlicht, H. J., R. Bartenschlager, and H. Schaller. 1989. The duck hepatitis B virus core protein contains a highly phosphorylated C-terminus that is essential for replication but not for RNA packaging. *J. Virol.* 63:2995–3000.

27. Seifer, M., and D. N. Standring. 1994. A protease-sensitive hinge linking the two domains of the hepatitis B virus core protein is exposed on the viral capsid surface. *J. Virol.* 68:5548–5555.

28. Guo, H., R. Mao, …, J. T. Guo. 2010. Production and function of the cytoplasmic deproteinized relaxed circular DNA of hepadnaviruses. *J. Virol.* 84:387–396.

29. Wang, J. C. Y., M. S. Dhason, and A. Zlotnick. 2012. Structural organization of pregenomic RNA and the carboxy-terminal domain of the capsid protein of hepatitis B virus. *PLoS Pathog.* 8:e1002919.

30. Chen, C., J. C.-Y. Wang, and A. Zlotnick. 2011. A kinase chaperones hepatitis B virus capsid assembly and captures capsid dynamics in vitro. *PLoS Pathog.* 7:e1002388.

31. Roseman, A. M., O. Borschukova, …, R. A. Crowther. 2012. Structures of hepatitis B virus cores presenting a model epitope and their complexes with antibodies. *J. Mol. Biol.* 423:63–78.

32. Yu, X., L. Jin, …, Z. H. Zhou. 2013. 3.5Å cryoEM structure of hepatitis B virus core assembled from full-length core protein. *PLoS ONE.* 8:e69729.

33. Wingfield, P. T., S. J. Stahl, …, A. C. Steven. 1995. Hepatitis core antigen produced in *Escherichia coli*: subunit composition, conformational analysis, and in vitro capsid assembly. *Biochemistry.* 34:4919–4932.

34. Ning, X., D. Nguyen, …, J. Hu. 2011. Secretion of genome-free hepatitis B virus—single strand blocking model for virion morphogenesis of para-retrovirus. *PLoS Pathog.* 7:e1002255.

35. Jiang, T., Z.-G. Wang, and J. Wu. 2009. Electrostatic regulation of genome packaging in human hepatitis B virus. *Biophys. J.* 96:3065–3073.

36. Meng, D., R. P. Hjelm, …, J. Wu. 2011. A theoretical model for the dynamic structure of hepatitis B nucleocapsid. *Biophys. J.* 101:2476–2484.

37. Zhang, D., R. Konecny, …, J. A. McCammon. 2004. Electrostatic interaction between RNA and protein capsid in cowpea chlorotic mottle virus simulated by a coarse-grain RNA model and a Monte Carlo approach. *Biopolymers.* 75:325–337.

38. Kolinski, A., A. Godzik, and J. Skolnick. 1993. A general method for the prediction of the three dimensional structure and folding pathway of globular proteins: application to designed helical proteins. *J. Chem. Phys.* 98:7420–7433.

39. Li, Z., J. Wu, and Z.-G. Wang. 2008. Osmotic pressure and packaging structure of caged DNA. *Biophys. J.* 94:737–746.

40. Bruss, V. 2004. Envelopment of the hepatitis B virus nucleocapsid. *Virus Res.* 106:199–209.

41. Wynne, S. A., R. A. Crowther, and A. G. W. Leslie. 1999. The crystal structure of the human hepatitis B virus capsid. *Mol. Cell.* 3:771–780.

42. Kegel, W. K., and Pv. Schoot Pv. 2004. Competing hydrophobic and screened-coulomb interactions in hepatitis B virus capsid assembly. *Biophys. J.* 86:3905–3913.

43. Kim, J., and J. Wu. 2014. A molecular thermodynamic model for the stability of hepatitis B capsids. *J. Chem. Phys.* 140:235101.

44. Li, Z., and J. Wu. 2006. Density functional theory for planar electric double layers: closing the gap between simple and polyelectrolytes. *J. Phys. Chem. B.* 110:7473–7484.

45. Li, Z., and J. Wu. 2006. Density functional theory for polyelectrolytes near oppositely charged surfaces. *Phys. Rev. Lett.* 96:048302.

46. Wu, J. Z. 2006. Density functional theory for chemical engineering: from capillarity to soft materials. *AIChE J.* 52:1169–1193.

47. Wu, J., and Z. Li. 2007. Density-functional theory for complex fluids. *Annu. Rev. Phys. Chem.* 58:85–112.

48. Jiang, T., Z. D. Li, and J. Z. Wu. 2007. Structure and swelling of grafted polyelectrolytes: predictions from a nonlocal density functional theory. *Macromolecules.* 40:334–343.

49. Gui, J. F., W. S. Lane, and X. D. Fu. 1994. A serine kinase regulates intracellular localization of splicing factors in the cell cycle. *Nature.* 369:678–682.

50. Colwill, K., L. L. Feng, …, X. D. Fu. 1996. SRPK1 and Clk/Sty protein kinases show distinct substrate specificities for serine/arginine-rich splicing factors. *J. Biol. Chem.* 271:24569–24575.

51. Yu, M., and J. Summers. 1994. Phosphorylation of the duck hepatitis B virus capsid protein associated with conformational changes in the C-terminus. *J. Virol.* 68:2965–2969.

52. Hilmer, J. K., A. Zlotnick, and B. Bothner. 2008. Conformational equilibria and rates of localized motion within hepatitis B virus capsids. *J. Mol. Biol.* 375:581–594.

53. Kann, M., A. Schmitz, and B. Rabe. 2007. Intracellular transport of hepatitis B virus. *World J. Gastroenterol.* 13:39–47.

54. Pugh, J., A. Zweidler, and J. Summers. 1989. Characterization of the major duck hepatitis B virus core particle protein. *J. Virol.* 63:1371–1376.

55. Melegari, M., S. K. Wolf, and R. J. Schneider. 2005. Hepatitis B virus DNA replication is coordinated by core protein serine phosphorylation and HBx expression. *J. Virol.* 79:9810–9820.

56. Zheng, Y., X. D. Fu, and J. H. J. Ou. 2005. Suppression of hepatitis B virus replication by SRPK1 and SRPK2 via a pathway independent of the phosphorylation of the viral core protein. *Virology.* 342:150–158.

57. Li, H.-C., E. Y. Huang, …, C. Shih. 2010. Nuclear export and import of human hepatitis B virus capsid protein and particles. *PLoS Pathog.* 6:e1001162.

58. Yeh, C. T., Y. F. Liaw, and J. H. Ou. 1990. The arginine-rich domain of hepatitis B virus precore and core proteins contains a signal for nuclear transport. *J. Virol.* 64:6141–6147.

59. Newman, M., P. K. Chua, …, C. Shih. 2009. Testing an electrostatic interaction hypothesis of hepatitis B virus capsid stability by using an in vitro capsid disassembly/reassembly system. *J. Virol.* 83:10616–10626.

60. Vanlandschoot, P., F. Van Houtte, …, G. Leroux-Roels. 2005. The arginine-rich carboxy-terminal domain of the hepatitis B virus core protein mediates attachment of nucleocapsids to cell-surface-expressed heparan sulfate. *J. Gen. Virol.* 86:75–84.

A theoretical study of SRPK interaction with the flexible domains of Hepatitis B capsids

Jehoon Kim and Jianzhong Wu

In this supporting material, we address key equations of the classical density functional theory (DFT) to predict the structure of Hepatitis B virus (HBV) capsids with regard to genome contents and phosphorylation process.

A. Density functional theory

The DFT provides accurate calculation on the thermodynamic potentials of free and tethered polyelectrolytes, as reported in comparison with experiment and simulation [1-6]. Within the coarse-grained model, the DFT has been applied for the equilibrium properties of HBV nucleocapsids with providing proper accounts for all important factors in the genome packaging [7, 8] as well as the structural change during the replication [9].

Here we present only the detailed DFT equations used for calculation of the radial distributions of viral components such as nucleic acids, C-terminal domain (CTD), and monomeric ions. The predicted density profiles can be determined by the modified-Poisson-Boltzmann equations:

$$\rho_\alpha(r) = \rho_\alpha^b \exp\left[\beta\mu_\alpha^{ex} - \beta\lambda_\alpha(r) \right], \tag{1}$$

$$\rho_p(r) = \frac{\exp[-\beta\lambda_p(r)]G^i(r)G^{M+1-i}(r)}{\int 4\pi r^2 dr \exp[-\beta\lambda_p(r)]G^i(r)G^{M+1-i}(r)}, \tag{2}$$

where $\beta = 1/(k_B T)$ with Boltzmann constant k_B and absolute temperature T; subscript α standing for a monomeric ion, p for a polymer segment of RNA and CTD; M denoting number of segments for the polymer chain; $\lambda_k(r)$ representing an effective one-body potential for a polyion segment or a monomeric ion; μ_α^{ex} denoting the excess chemical potential of monomeric

ions, which is determined by the mean-spherical approximation (MSA) for the electrolyte at the bulk concentration ρ_α^b [10]. In equation (2), $G^i(r)$ is a chain propagator function (i.e., Green function), which is to be described by the recursive relation:

$$G^i(r) = \frac{1}{2\sigma_p r} \int_{|\sigma_p - r|}^{r+\sigma_p} dr' \exp[-\beta\lambda_p(r')] G^{i-1}(r') r'$$ (3)

for $i = 2, \cdots, M$ while $G^1(r) = 1$, with σ_p denoting the segment diameter.

The one-body potential ($\lambda_k(r)$) represents the non-ideal thermodynamic property due to intermolecular interactions. Such a non-ideality is due to the external potential $\varphi_k(r)$ originated by the capsid wall, the mean electrostatic potential $\psi(r)$, and the local excess chemical potential from excluded volume and correlation effects $\mu_{hsc}^{ex}(r)$:

$$\lambda_k(r) = \varphi_k(r) + Z_k e\psi(r) + \mu_{hsc}^{ex}(r),$$ (4)

where Z_k denotes the electric valence of each particle k with the unit electronic charge e. In a reduced form, the mean electrostatic potential is:

$$\psi^*(r) \equiv \beta e\psi(r) = \psi^*(r=0) - 4\pi l_B \int_0^r dr'(r' - \frac{r'^2}{r}) \sum_{k=p,+,-} Z_k \rho_k(r').$$ (5)

The value of $\psi^*(r=0)$ is evaluated by applying the other boundary condition that $\psi(r=\infty)=0$, and the Bjerrum length $l_B = 0.78$ nm is applied where the electrostatic potential is to be equal to the thermal energy $k_B T$.

The local excess chemical potential is determined by a functional derivative of the excess Helmholtz energy (F_{hsc}^{ex}) due to the excluded volume and correlation effects with respect to the one-body density:

$$\mu_{hsc}^{ex}(r) = \frac{\delta F_{hsc}^{ex}}{\delta \rho_k(r)}. \tag{6}$$

Such the excess Helmholtz energy functional can be estimated from inter-related contributions of the excess Helmholtz energy functional due to hard-sphere exclusion (F_{hs}^{ex}), the effect of chain connectivity on the intramolecular correlations (F_{ch}^{ex}), and the hard-sphere and electrostatic correlations (F_{el}^{ex}):

$$F_{hsc}^{ex} = F_{hs}^{ex} + F_{ch}^{ex} + F_{el}^{ex}. \tag{7}$$

The contribution by hard-sphere repulsions on the Helmholtz energy functional is determined by the modified fundamental measure theory (FMT) [11, 12]:

$$\beta F_{hs}^{ex} = \int d\mathbf{r}\{-n_0 \ln(1-n_3) + \frac{n_1 n_2 - \mathbf{n_{V1} n_{V2}}}{1-n_3}$$
$$+ \frac{1}{36\pi}[n_3 \ln(1-n_3) + \frac{n_3^2}{(1-n_3)^2}]\frac{(n_2^3 - 3n_2\mathbf{n_{V2} n_{V2}})}{n_3^3}\} \tag{8}$$

where $\{n_\alpha, \alpha = 1,2,3,V1,V2\}$ stand scalar and vector weighted densities as defined in the original version of the FMT [13].

The excess Helmholtz energy due to the intra-chain and electrostatic correlations is related with the chain connectivity of the polymeric segments [14]. Following the extension of first-order thermodynamic perturbation theory (TPT1) [15], the intra-chain correlation is obtained :

$$\beta F_{ch}^{ex} = \frac{1-M}{M}\int n_{0p}\zeta_p \ln y(\sigma_p, n_\omega) d\mathbf{r}, \tag{9}$$

where $\zeta_p = 1 - \mathbf{n_{V2p} n_{V2p}}/n_{2p}^2$ describes the effect of local density variation, and $y(\sigma_p, n_\omega)$ presents the contact value of the cavity correlation function (CCF) of segments. According to

the mean-spherical approximation (MSA) theory for monomeric electrolyte solutions [10], $y(\sigma_p, n_\omega)$ is evaluated:

$$y(\sigma_p, n_\omega) = \left[\frac{1}{1-n_3} + \frac{n_2 \sigma_p (1 - \mathbf{n_{V2}} \mathbf{n_{V2}} / n_2^2)}{4(1-n_3)^2} \right] \exp\left(-\frac{\Gamma^2 a_p^2}{4\pi^2 l_B \sigma_p} \right) \exp\left(\frac{l_B Z_p^2}{\sigma_p} \right), \tag{10}$$

where parameter of Γ and a_p are described as

$$\Gamma = \sqrt{\pi l_B \sum_{k=p,+,-} n_{0k} \left(\frac{1}{1+\Gamma \sigma_k} \right)^2 \left(Z_k - \frac{\pi P_n \sigma_k^2}{2(1-n_3)} \right)^2}, \tag{11}$$

$$a_p = \frac{2\pi l_B \left(Z_p - \frac{\pi P_n \sigma_p^2}{2(1-n_3)} \right)}{\Gamma(1+\Gamma\sigma_p)} \tag{12}$$

with

$$P_n = \sum_{k=p,+,-} \frac{2n_{1k} Z_k}{1+\Gamma\sigma_k} \bigg/ \left(1 + \frac{3}{(1-n_3)} \sum_{k=p,+,-} \frac{n_{3k}}{1+\Gamma\sigma_k} \right). \tag{13}$$

In addition, the excess Helmholtz energy due to electrostatic correlations is estimated by the hypernetted chain approximation (HNC). It has been shown that HNC provide sufficient evaluation of the long-ranged electrostatic correlations [16, 17]. Accordingly, the excess Helmholtz energy is represented by a quadratic functional expansion with respect to the property for a bulk fluid with uniform densities $\{\rho_i^b\}$:

$$\beta F_{el}^{ex} = \beta F_{el}^{ex}[\{\rho_i^b\}] - \int d\mathbf{r} \sum_{i=p,+,-} \Delta C_i^{(1)el} (\rho_i(\mathbf{r}) - \rho_i^b)$$
$$-\frac{1}{2} \int\int d\mathbf{r} d\mathbf{r}' \sum_{i,j=p,+,-} \Delta C_{ij}^{(2)el} (|\mathbf{r} - \mathbf{r}'|)(\rho_i(\mathbf{r}) - \rho_i^b)(\rho_j(\mathbf{r}') - \rho_j^b) \tag{14}$$

where $\Delta C_i^{(1)el}$ and $\Delta C_{ij}^{(2)el}$ denote the first- and second-order direct correlation functions (DCF) related with the electrostatic interactions in the reference system. We apply the MSA to the expressions for the DCF [10].

B. Numerical implementation

The density distributions of viral components are predicted through above equations and applying the Picard iteration method. From an input from guessing on the density profiles, we obtain relevant quantities such as the reduced electrostatic potential ($\psi^*(r)$), the effective one-body potential for particles ($\lambda_k(r)$), and the Green function ($G^i(r)$). In corresponding to those obtained values, new density profiles are selected as updated input. The change between input and output profiles is accessed, and the iteration cycle is continued until the variance on density distribution of monomeric ions and polyions at all positions converges into smaller than 0.01%.

References

1. Jiang, T., Z.D. Li, and J.Z. Wu, *Structure and swelling of grafted polyelectrolytes: Predictions from a nonlocal density functional theory.* Macromolecules, 2007. **40**(2): p. 334-343.
2. Li, Z.D. and J.Z. Wu, *Density-functional theory for polyelectrolytes near an oppositely-charged surface.* Physical Review Letters, 2006. **96**: p. 048302.
3. Li, Z.D. and J.Z. Wu, *Density functional theory for planar electric double layers: Closing the gap between simple and polyelectrolytes.* Journal of Physical Chemistry B, 2006. **110**: p. 7473-7484.
4. Wu, J.Z. and T. Jiang, *Ionic effects in collapse of polyelectrolyte brushes.* Journal of Physical Chemistry B, 2008. **112**(26): p. 7713-7720.
5. Jiang, T. and J.Z. Wu, *Self-organization of multivalent counterions in polyelectrolyte brushes.* Journal of Chemical Physics, 2008. **129**(8): p. 10.1063/1.2966359.
6. Wang, L., H.J. Liang, and J.Z. Wu, *Electrostatic origins of polyelectrolyte adsorption: Theory and Monte Carlo simulations.* Journal of Chemical Physics, 2010. **133**(4): p. 10.1063/1.3463426.
7. Jiang, T., Z.G. Wang, and J.Z. Wu, *Electrostatic Regulation of Genome Packaging in Human Hepatitis B Virus.* Biophysical Journal, 2009. **96**(8): p. 3065-3073.
8. Li, Z.D., J.Z. Wu, and Z.G. Wang, *Osmotic pressure and packaging structure of caged DNA.* Biophysical Journal, 2008. **94**(3): p. 737-746.

9. Meng, D., et al., *A theoretical model for the dynamic structure of hepatitis B nucleocapsid.* Biophysical Journal, 2011. **101**(10): p. 2476-2484.

10. Blum, L., *Mean spherical model for asymmetric electrolytes .1. Method of solution.* Molecular Physics, 1975. **30**(5): p. 1529-1535.

11. Yu, Y.X. and J.Z. Wu, *Structures of hard sphere fluids from a modified fundamental measure theory.* Journal of Chemical Physics, 2002. **117**(22): p. 10156-10164.

12. Roth, R., et al., *Fundamental measure theory for hard-sphere mixtures revisited: the White Bear version.* Journal of Physics-Condensed Matter, 2002. **14**(46): p. 12063-12078.

13. Rosenfeld, Y., *Free-energy model for the inhomogeneous hard-sphere fluid mixture and density-functional theory of freezing.* Physical Review Letters, 1989. **63**(9): p. 980-3.

14. Chandler, D. and L.R. Pratt, *Statistical mechanics of chemical equilibria and intramolecular structures of nonrigid molecules in condensed phases.* Journal of Chemical Physics, 1976. **65**(8): p. 2925-40.

15. Yu, Y.X. and J.Z. Wu, *Density functional theory for inhomogeneous mixtures of polymeric fluids.* Journal of Chemical Physics, 2002. **117**(5): p. 2368-2376.

16. Yu, Y.X., J.Z. Wu, and G.H. Gao, *Density-functional theory of spherical electric double layers and zeta potentials of colloidal particles in restricted-primitive-model electrolyte solutions.* Journal of Chemical Physics, 2004. **120**(15): p. 7223-7233.

17. Li, Z.D. and J.Z. Wu, *Density-functional theory for the structures and thermodynamic properties of highly asymmetric electrolyte and neutral component mixtures.* Physical Review E, 2004. **70**(3): p. 031109.